J. Fluid Mech. (2002), *vol.* 455, *pp.* 1–19.
DOI: 10.1017/S0022112001007297 Printed in the United Kingdom

Secondary motion in convection layers generated by lateral heating of a solute gradient†

By CHO LIK CHAN, WEN-YAU CHEN AND C. F. CHEN

Department of Aerospace and Mechanical Engineering, The University of Arizona, Tucson, AZ, 85721 USA

(Received 22 May 2000 and in revised form 5 March 2001)

The three-dimensional motion observed by Chen & Chen (1997) in the convection cells generated by sideways heating of a solute gradient is further examined by experiments and linear stability analysis. In the experiments, we obtained visualizations and PIV measurements of the velocity of the fluid motion in the longitudinal plane perpendicular to the imposed temperature gradient. The flow consists of a horizontal row of counter-rotating vortices within each convection cell. The magnitude of this secondary motion is approximately one-half that of the primary convection cell. Results of a linear stability analysis of a parallel double-diffusive flow model of the actual flow show that the instability is in the salt-finger mode under the experimental conditions. The perturbation streamlines in the longitudinal plane at onset consist of a horizontal row of counter-rotating vortices similar to those observed in the experiments.

1. Introduction

When a tank of fluid that is stably stratified by a solute gradient is heated from one side, the primary convective motion, which consists of a series of nearly horizontal convection cells, is generated by double-diffusive effects when the critical condition is exceeded. The first systematic study of this phenomenon was carried out by Thorpe, Hutt & Soulsby (1969). They conducted experiments in a tall, narrow tank filled with stably stratified salt solution. The horizontal temperature difference across the tank was slowly increased until the onset of a vertical array of convection cells all along the tank. A linear stability analysis was carried out for the asymptotic state of very large solute Rayleigh numbers, the conditions under which the experiments were conducted. Good agreement was obtained between the stability predictions and the experimental observations. Chen, Briggs & Wirtz (1971) studied the stability of a solute gradient subjected to impulsive lateral heating in a wide tank. In their experiments, they observed simultaneous onset of convection cells at the hot wall and subsequent intrusion into the fluid interior when the critical condition was exceeded. In their problem, the natural length scale was the height rise, h, of a heated parcel of fluid in the initially stratified fluid, defined as $h = \alpha\Delta T/(-\beta \mathrm{d}S/\mathrm{d}z)$, in which α and β are the volumetric expansion coefficients due to heat and solute, respectively. In a series of 15 experiments, they determined the critical condition in terms of a Rayleigh number, R_h, based on the length scale h for onset of instability to be $15\,000 \pm 2500$. They also determined that the average thickness of the convection layer is proportional to h. For the Rayleigh number range investigated, $1.4 \times 10^4 < R_h < 5.4 \times 10^4$,

† With an Appendix by O. S. Kerr.

the layer thickness varied from $0.67h$ to $0.97h$. Later investigations by Huppert & Turner (1980) and Huppert, Kerr & Hallworth (1984) found that the cell thickness decreases as R_h increases and asymptotes to $0.6h$ at $R_h \simeq 10^6$–10^9. There have been a number of interesting experimental investigations, stability analyses, and numerical simulations of similar double-diffusive problems since the 1970s. For a review of such work, see Chen & Chen (1997) and Chen (1999). It is worth noting that all the stability analyses and numerical simulations were carried out assuming two-dimensional motion.

Within each convection cell, there is a counterflow of relatively warm and solute-rich fluid over colder and solute-poor fluid, a situation conducive to the onset of salt-finger instability. Such instabilities will cause secondary motion in the longitudinal plane perpendicular to the temperature gradient. This phenomenon was observed by Chen & Chen (1997) by flow visualization in the horizontal plane. The seeded particles collect into bands aligned in the flow direction, and these bands are generated as soon as the primary convection cells are formed. Such three-dimensional motion was also observed by Biello (1997).

Stimulated by the observations of three-dimensional motion in these convection cells, Kerr (2000) extended his earlier two-dimensional stability analysis of steady double-diffusive interleaving intrusions (Kerr 1992) by seeking possible three-dimensional instabilities in such flows. In order to make the problem tractable, he considered a steady basic state in a constant-thickness intrusion parallel to the fastest-growing nodes. Results show that three-dimensional instabilities exist in the form of cells in the longitudinal plane perpendicular to the direction of intrusion and such instabilities are slightly more unstable than the two-dimensional instabilities under suitable conditions.

Recently, we performed experiments to obtain visualizations of the secondary motion as well as quantitative velocity measurements by PIV. The visualizations are images of particle traces in the transverse plane (parallel to the initial temperature gradient and the gravity vector) and in the longitudinal plane (perpendicular to the initial temperature gradient and the gravity vector). The former shows the primary motion and the latter the secondary motion in each convection cell. The results show that the secondary motion in the longitudinal plane consists of a horizontal row of vortices with axes aligned in the direction of the temperature gradient. Velocity vectors were obtained by analysing the particle images by PIV. Results show that the velocity magnitude of the secondary motion is approximately one-half that of the primary motion.

In order to gain an understanding of the instability mechanisms that caused the secondary motion, a linear stability analysis was carried out for a steady, parallel double-diffusive flow model approximating the primary motion in a convection cell. The analysis was made separately in the longitudinal and transverse planes. The results show that the instability in both planes may onset in either the diffusive or the salt-finger mode. For a fluid with a large Lewis number, such as the salt-water solution, salt-finger instability is the most critical mode. Furthermore, the stability boundary for the salt-finger mode in the longitudinal plane is very close to that in the transverse plane, in agreement with the findings of Kerr (2000). Perturbation streamlines in the longitudinal plane at onset show a horizontal row of counter-rotating vortices in the middle of the cell, and the critical wavelength is in general agreement with the observations. In the following, the experimental investigation and the stability analysis are presented in detail, followed by a summary and conclusions.

2. Experiments

2.1. *Apparatus and procedures*

The experiments were carried out in a tank 5 cm wide × 9.5 cm high × 9.5 cm long, the same tank used by Chen & Chen (1997) with one modification. One of the 9.5 cm × 9.5 cm copper sidewalls was replaced by a Plexiglas wall for flow visualization purposes. The fluid was a stratified salt solution with the initial concentration of the fluid varying from 2% to 5% salt. The stratification was achieved by successively introducing 21 equal volumes of solutions with decreasing salt content into the tank. The solution was seeded with 10 μm diameter particles for flow visualization. The procedure is described in detail in Chen & Chen (1997). Once the tank was filled, a Plexiglas cover was placed on top of the tank in contact with the solution to prevent evaporation. The tank was left standing for one hour to allow diffusion to smooth out the salt gradient before the start of the experiment.

To initiate the experiment, the temperature of the copper wall was brought to 6 °C above that of the fluid in the tank by circulating pre-heated liquid from a constant-temperature bath. For flow visualization, a light sheet generated by a 1.5 W Argon ion laser together with a cylindrical lens can be placed either parallel (transverse view) or perpendicular (longitudinal view) to the temperature gradient. The particles illuminated by the light sheet were imaged by a CCD camera and displayed on a monitor and the data were recorded on a tape. Time-lapse photographs were taken of the particle images, and the recorded data were later processed by MACPIV† software to obtain velocity vectors and constant vorticity contours. The thickness of the light sheet was 0.3 cm in the transverse plane and 1.0 cm in the longitudinal plane in order to capture the particles within the light sheet for a reasonable period of time. Different experiments with identical conditions were run to obtain images in the transverse and longitudinal planes and shadowgraphs in the transverse plane.

2.2. *Results*

Since the temperature of the Plexiglas wall opposite the heating wall was not controlled, it is important that data should be taken at early stages of the experiment. The results presented here are all from the data taken within the first 10 min of the experiment when the convection cells reached halfway across the tank. Although particle-trace images were monitored and stored for approximately 30 min into each experiment, the data for the last 20 min were for observation purposes only.

Shadowgraphs and particle trace images in the transverse plane and longitudinal plane are shown in figures 1(*a*), 1(*b*), and 1(*c*), respectively, at 4, 6, and 9 min after the start of the experiment. The shadowgraphs (figure 1*a*) show the entire tank with heating from the left wall. The particle trace images were obtained with time exposures of 4 s and the field of view was enlarged by placing a magnifying lens in front of the test tank. The dimension of the images in the transverse plane is 2.8 cm high × 2.0 cm wide, with the heating wall appearing on the right. The dimensions for the images in the longitudinal plane are 1.8 cm high × 2.3 cm wide. These dimensions were determined by placing a lined grid in the tank prior to filling it with fluid.

The shadowgraphs in figure 1(*a*) show that, at 4 min, there were 15 convecting layers and, by 6 min, the number of layers decreased to 11 due to the merging of some layers. These layers had advanced to approximately the middle of the tank by 9 min. It is noted that the same number of convecting layers persisted for 30 min

† MACPIV was developed by Professor Jeffrey Jacobs and his students and is briefly described in a paper by Zuercher, Jacobs & Chen (1998).

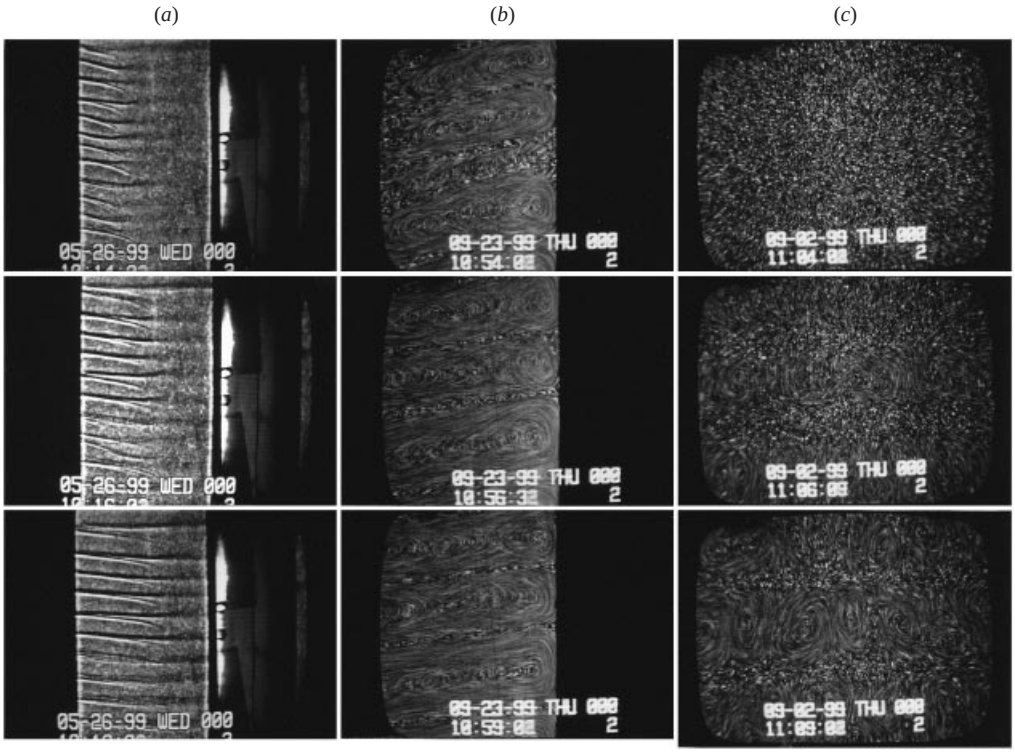

FIGURE 1. Flow visualization at 4 min, 6 min, and 9 min (from top to bottom) into the experiments: (*a*) shadowgraph; (*b*) particle trances in the transverse plane; (*c*) particle traces in the longitudinal plane.

before any further merging took place. The particle traces in the transverse plane (figure 1*b*) show four convecting cells above the date marker at 4 min, with one of the layers being merged into its neighbours. At 6 min, there were only three vigorously convecting layers remaining. Circulation in each of the cells had intensified at 9 min. The particle trace images in the longitudinal plane are shown in figure 1(*c*). The centre of the 1 cm thick laser sheet was located at 1.25 cm from the heating surface. For this much enlarged view, the image of the lined grid placed in the tank prior to the start of the experiment showed that aberrations of the image were present in the peripheral areas. Only the central region above the date marker is aberration free. Motion in the longitudinal plane was first detected at 4 min, as indicated by lateral movements of particles above the marker. At 6 min, vortices were forming in the central row and, by 9 min, they were well developed with axes parallel to the temperature gradient.

The images in the transverse and longitudinal planes at 9 min were processed by MACPIV and the results are shown in figures 2 and 3. The image, the velocity vectors, and the constant vorticity contours are shown in each of the figures, with black and grey lines denoting positive and negative vorticity, respectively. It is seen that the velocity magnitudes in the transverse plane are generally about twice as large as those in the longitudinal plane. The maximum magnitudes for these two cases are 16.6 mm s^{-1} and 7.3 mm s^{-1}, while the average magnitudes of all the velocity vectors evaluated are 5.4 mm s^{-1} and 2.1 mm s^{-1}. These results show that the flow is three-dimensional in nature and should be properly accounted for in any numerical simulations of the problem.

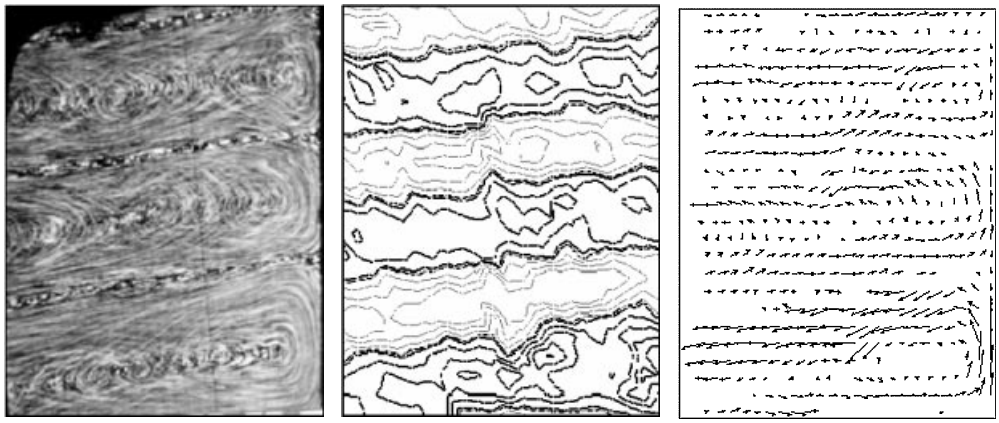

FIGURE 2. Flow image, vorticity contours and velocity vectors, in the transverse plane at $t = 9$ min.

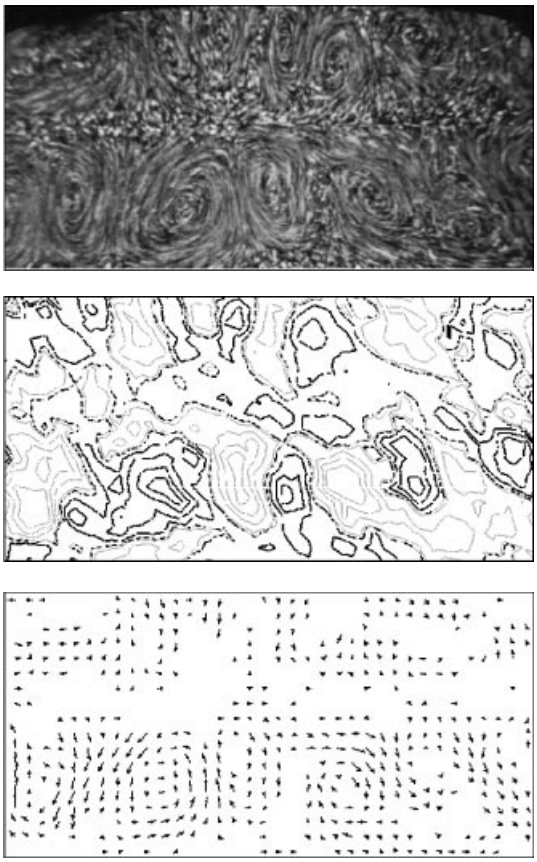

FIGURE 3. Flow image, vorticity contours and velocity vectors, in the longitudinal plane at $t = 9$ min.

The primary convection in the transverse plane consists of nearly horizontal elongated convection cells advancing toward the cold wall. For the secondary flow in the longitudinal plane, the image was cropped to 1.15 cm high $\times$ 2.3 cm wide, showing only two layers. There are four pairs of vortices in the bottom row, with an average

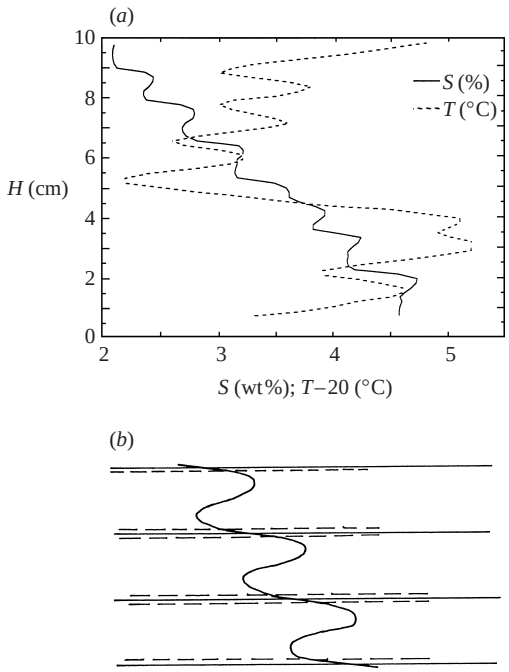

FIGURE 4. (*a*) Vertical temperature and solute concentration distribution 39 min into an experiment with $\Delta T = 10\,^{\circ}\mathrm{C}$ from Chen & Chen (1997). (*b*) Idealized temperature and solute concentration distribution for the parallel flow model. Interfacial regions are bordered by dashed lines.

wavelength of 0.5 cm. The thickness of the layer is 0.6 cm, yielding a wavelength-to-thickness ratio of $\lambda/D = 0.83$. By the way, Chen & Chen (1997) observed that there were usually approximately 20 particle bands in a cross-sectional area of $5\,\mathrm{cm} \times 9.5\,\mathrm{cm}$, in agreement with the present observations.

3. Stability analysis

3.1. *Idealized flow model*

The experimental results were obtained in a transient state as the primary convection cells were advancing toward the cold wall. But even at this early stage, the flow away from the hot wall is relatively warmer and richer in solute than the return flow. It is reasonable to expect that this particular vertical distribution of temperature and solute concentration is the cause of the instability that eventually develops into the secondary flow observed in the experiment. To render the problem amenable to a linear stability analysis while retaining the essential physics of the problem, we consider the fully developed double-diffusive convection in each of the convection cells.

When the flow is fully developed, the tank is filled by a vertical array of nearly horizontal convection cells. In each of the cells, the flow in the upper (lower) half is away from (toward) the hot wall and it is warmer (cooler) and solute rich (poor). The solute concentration and temperature distributions in such a fully developed cellular flow have been obtained by Chen & Chen (1997) and are shown in figure 4(*a*). These measurements were made at 39 min into an experiment with an initial solute gradient of $-0.316\%\,\mathrm{cm}^{-1}$ (the same as in the present experiments) and a maintained

10 °C lateral temperature difference. Focusing our attention on the regular layers in the upper half of the tank just above the merging layers, the solute concentration shows that each cell is bordered above and below by interfacial layers with large concentration gradients. Within these borders, the concentration is S-shaped. The overall distribution shows a negative vertical gradient, reflecting the initial value. The overall temperature distribution shows a slight positive gradient due to sideways heating and is S-shaped within each cell. It is noted here that there was a slight vertical displacement between the temperature and salinity probes.

Within each cell, the fluid flowing away from the hot wall along the top is continuously losing heat and solute to the counterflowing fluid in the cell above. The converse is true for the fluid flowing from the cold wall at the bottom of each cell. Therefore, along both boundaries, the velocity is zero, and both temperature and concentration decrease from the hot to the cold wall. In this idealized model, we assume both gradients are equal and constant.

Furthermore, we assume that the overall vertical concentration gradient in the tank is completely taken up by the interfacial regions, while the solute concentration of the fluid within each cell, away from the boundaries, varies about a mean value, as shown in figure 4(*b*). With this assumption, we neglected the small vertical concentration gradient within each cell, as shown by the measurement in figure 4(*a*). In addition, we neglected the background vertical temperature gradient. With these simplifications, the idealized model for each convecting cell consists of a long, shallow, rigid cell differentially heated and salted at the two ends. Along the upper and lower boundaries, both temperature and concentration increase linearly from the cold to the hot end.

The temperature difference, ΔT, between the two ends of the cell is the experimental value. The concentration difference, ΔS, between the two ends is proportional to the vertical concentration difference across each cell, which may be approximated by $(S_L - S_U)/N$, where S_L and S_U are the initial solute concentration at the lower and upper boundaries of the vertical tank and N is the total number of cells. We analyse the linear stability of the parallel flow existing in the midsection of the tank for values of ΔT and ΔS and the fluid properties Pr and Le.

This parallel flow model was used by Hart (1972) to consider the stability of thin, non-rotating Hadley circulation. Later, Jeevaraj & Imberger (1991) used the same model to estimate the velocity distribution in double-diffusive intrusions generated in the same manner as in our experiments. In their calculations, the horizontal solute gradient was neglected. Their ultimate purpose was to estimate the speed of advance of the intrusions. The theoretical and experimental velocity distributions, as well as the speed of advancement of the intrusion agreed well with each other. With their results in mind, we assume our model will work just as well in the developing cells.

We note here that, in actual experiments, the thickness of each convection cell for a given initial concentration gradient is proportional to ΔT (Chen *et al.* 1971), therefore ΔT and ΔS for our model are not independent. In the stability analysis, we regard them as independent quantities in order to determine the stability boundary, from which the stability characteristics of the actual convection cells can then be ascertained.

3.2. *Analysis*

Consider a shallow horizontal tank of thickness d and length L with temperature and solute concentrations maintained at T_0 and S_0 at the left end and $T_0 + \Delta T$ and $S_0 + \Delta S$ at the right end. Let the origin of a Cartesian coordinate system be at the centre of the tank, with x in the direction of the positive temperature gradient, and

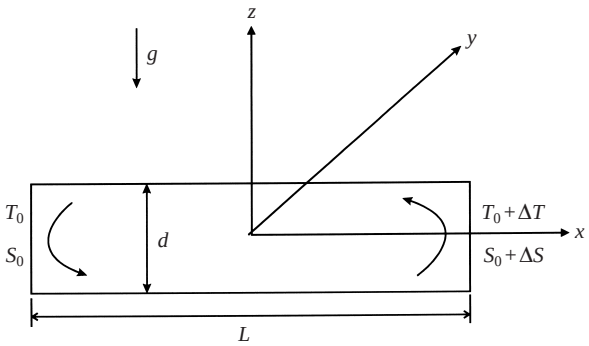

FIGURE 5. Sketch of the model double-diffusive flow.

z vertically upward, as shown in figure 5. Linear distributions of temperature and solute concentration are maintained along the rigid upper and lower boundaries with constant slopes $\gamma = \Delta T/L$ and $\gamma_S = \Delta S/L$.

The fluid is assumed to be Boussinesq and its density is linear in both temperature and solute concentration, $\rho = \rho_0(1-\alpha(T-T_0)+\beta(S-S_0))$, in which $\alpha = -\rho_0^{-1}\partial\rho/\partial T$ and $\beta = \rho_0^{-1}\partial\rho/\partial S$. The non-dimensional governing equations are

$$\nabla \cdot \boldsymbol{V} = 0, \tag{1}$$

$$\frac{\partial \boldsymbol{V}}{\partial t} + Gr(\boldsymbol{V}\cdot\nabla)\boldsymbol{V} = -Gr\nabla p + \boldsymbol{k}\left(T - \frac{Gs}{Gr}S\right) + \nabla^2\boldsymbol{V} \tag{2}$$

$$Pr\frac{\partial T}{\partial t} + Gr\,Pr(\boldsymbol{V}\cdot\nabla)T = \nabla^2 T, \tag{3}$$

$$Le\,Pr\frac{\partial S}{\partial t} + Le\,Gr\,Pr(\boldsymbol{V}\cdot\nabla)S = \nabla^2 S. \tag{4}$$

The thermal and solute Grashof numbers, Gr and Gs, and the Prandtl and Lewis numbers are defined as

$$Gr = \frac{g\alpha\gamma d^4}{\nu^2}, \quad Gs = \frac{g\beta\gamma_S d^4}{\nu^2}, \quad Pr = \frac{\nu}{\kappa}, \quad Le = \frac{\kappa}{\kappa_s},$$

in which g is the gravitational acceleration, ν is the kinematic viscosity, κ is the thermal diffusivity, and κ_S is the mass diffusivity. The characteristic length, time, velocity, pressure, temperature, and solute concentration are d, d^2/ν, $g\alpha\gamma d^3/\nu$, $\rho_0(g\alpha\gamma d^3/\nu)^2$, γd, and $\gamma_S d$, respectively. The boundary conditions along the top and bottom wall are

$$\boldsymbol{V} = 0, \quad T = x, \quad S = x, \quad \text{at} \quad z = \pm\tfrac{1}{2}. \tag{5}$$

For the basic state with steady parallel flow, $\boldsymbol{V}_b = (u_b(z), 0, 0)$, $T_b = T_b(x,z)$, and $S_b = S_b(x,z)$, the solution are

$$u_b = \frac{1}{6}\left(1 - \frac{Gs}{Gr}\right)F(z), \tag{6}$$

$$T_b = x + \frac{Gr\,Pr}{6}\left(1 - \frac{Gs}{Gr}\right)G(z), \tag{7}$$

$$S_b = x + \frac{Le\,Gr\,Pr}{6}\left(1 - \frac{Gs}{Gr}\right)G(z), \tag{8}$$

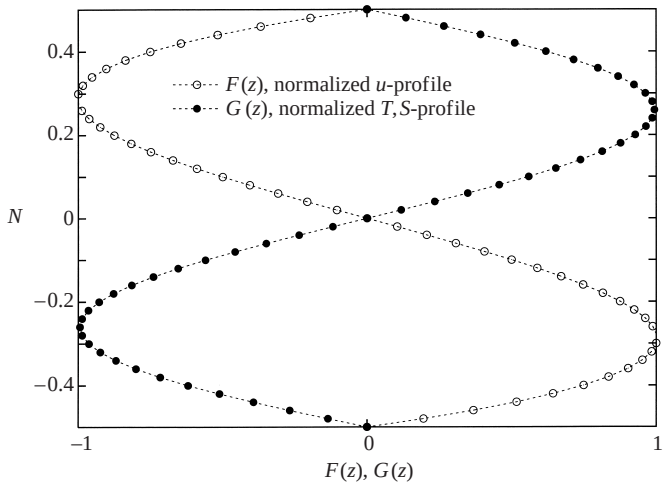

FIGURE 6. Normalized basic-state velocity u_b represented by $F(z)$, and temperature T_b and solute concentration S_b represented by $G(z)$.

$$F(z) = z\left(z^2 - \tfrac{1}{4}\right), \tag{9}$$

$$G(z) = \frac{z^5}{20} - \frac{z^3}{24} + \frac{7z}{960}. \tag{10}$$

The vertical distributions of $F(z)$, the normalized velocity, and $G(z)$, the normalized temperature and solute concentration, are shown in figure 6, both functions being normalized with their respective maximum values. The temperature distribution is stable in the middle of the fluid layer but unstable in the two layers bordering the upper and lower boundaries. Hart (1972) analysed the linear stability of the thermal convection problem ($S = 0$) with respect to transverse disturbances confined in the (x, z)-plane or longitudinal disturbances confined in the (y, z)-plane separately. The more recent stability considerations of Kuo *et al.* (1986) show that, for $0.14 < Pr < 0.45$, the most critical instability is in the transverse mode and, for $Pr > 0.45$, it is in the longitudinal mode. In both cases, the instability consists of two rows of counter-rotating cells, one each near the horizontal boundaries. It is noted that the relative magnitudes of Gs and Gr determine the direction of the flow.

With the addition of a horizontal solute gradient, γ_S, the following three possible modes of instability arise. For small γ_S, the unstable regions found in the thermal convection case become stabilized by the solute gradient. The mode of instability remains steady convection. As γ_S is increased, the mode of instability will become double diffusive in these regions and onsets in the oscillatory mode. The third possibility is the onset of a salt-finger instability mode occurring in the middle section of the fluid layer where the vertical temperature gradient is stabilizing but the solute gradient is destabilizing. We hope to determine the effects of the competitive interactions among the various modes of instability by the following stability analysis.

We analyse the stability characteristics in the longitudinal and transverse modes separately, with a more-detailed presentation of the former. For the longitudinal mode, the perturbation quantities denoted by primes are assumed to be periodic in

the y-direction:

$$\begin{pmatrix} u' \\ v' \\ w' \\ p' \\ T' \\ S' \end{pmatrix} = \begin{pmatrix} u(z) \\ v(z) \\ w(z) \\ p(z) \\ T(z) \\ S(z) \end{pmatrix} \exp(\sigma t + \mathrm{i}ky) \tag{11}$$

in which k is the wavenumber. When these are substituted into the linearized equation, and with some manipulations, we obtain the following stability equations:

$$[(\mathrm{D}^2 - k^2) - \sigma](\mathrm{D}^2 - k^2)w = k^2 \left(T - \frac{Gs}{Gr} S \right), \tag{12}$$

$$[(\mathrm{D}^2 - k^2) - Pr\sigma]T = Gr\,Pr(u + T_{bz}w), \tag{13}$$

$$[(\mathrm{D}^2 - k^2) - Le\,Pr\sigma]S = Le\,Gr\,Pr(u + S_{bz}w), \tag{14}$$

$$[(\mathrm{D}^2 - k^2) - \sigma]u = Gr\,u_{bz}w, \tag{15}$$

in which $\mathrm{D} = \mathrm{d}/\mathrm{d}z$, and T_{bz}, S_{bz}, and u_{bz} denote the vertical gradients T, S, and u in the basic flow.

A similar set of stability equations are derived for the transverse mode. In this case, perturbation quantities are assumed to be $u' = u(z)\exp(\sigma t + \mathrm{i}lx)$, etc. The non-dimensional wavenumber in the x-direction is denoted by l. The equations are

$$[(\mathrm{D}^2 - l^2) - \sigma][\mathrm{D}^2 - l^2]w = l^2 \left[T - \frac{Gs}{Gr} S \right] + \mathrm{i}l[u_b(\mathrm{D}^2 - l^2)w - wu_{bz}^2], \tag{16}$$

$$[(\mathrm{D}^2 - l^2) - Pr\sigma]T = Gr\,Pr \left(\mathrm{i}lu_b T + \frac{\mathrm{i}\mathrm{D}w}{l} + T_{bz}w \right), \tag{17}$$

$$[(\mathrm{D}^2 - l^2) - Pr\sigma]S = Le\,Gr\,Pr \left(\mathrm{i}lu_b S + \frac{\mathrm{i}\mathrm{D}w}{l} + S_{bz}w \right). \tag{18}$$

Only three equations are needed here because u can be expressed in terms of w by the continuity equation in the transverse mode. These equations are solved by the Galerkin method with u and w expanded into Chandrasekhar (1961) functions and T and S into trigonometric functions. Converged solutions are obtained with 16 Galerkin expansion terms.

3.3. *Results for the longitudinal model*

The experiments were performed using a salt solution at a mean temperature of 27 °C with $Pr = 5.83$ and $Le = 94.2$. The cell dimensions at the time of PIV measurement are $L \approx 2.8$ cm and $d \approx 0.6$ cm. We now assume that, for $L/d = 4.7$, the parallel flow model will give a good estimate of the actual flow structure. With $\Delta T = 6\,^{\circ}\mathrm{C}$, $\alpha = 2.76 \times 10^{-4}\,^{\circ}\mathrm{C}^{-1}$, and $\nu = 0.86 \times 10^{-2}\,\mathrm{cm}^2\,\mathrm{s}^{-1}$, the experimental $Gr = 1021$. At this time, there were eleven layers in the tank. The average ΔS across each layer is $\sim 0.27\%$. As shown by Jeevaraj & Imberger (1991), the intrusion ends in a region where the fluid is essentially unperturbed with the initial solute gradient. We assume the solute concentration at the hot wall is equal to that along the bottom of the layer, and the concentration at the end of the intrusion is the mean concentration of the layer. Then, $\Delta S \sim 0.14\%$, and with $\beta = 0.0072\%^{-1}$ the experimental $Gs = 603$. The stability calculations are done with $Pr = 7$ and $Le = 3$ and 100. We carried out

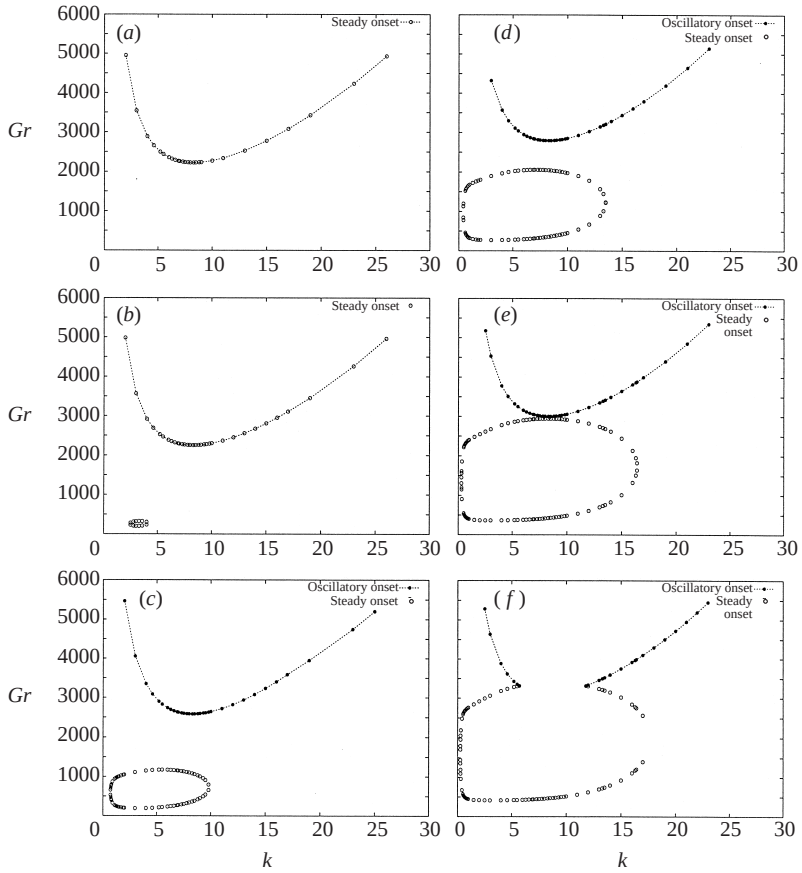

FIGURE 7. Marginal stability curves for the longitudinal mode for $Le = 3$ at increasing values of Gs: (*a*) 55, (*b*) 60, (*c*) 150, (*d*) 250, (*e*) 350, and (*f*) 400. Note the increase of the salt-finger instability bubble.

calculations for $Le = 3$ because it converges much faster than the $Le = 100$ case and the stability characteristics can be mapped clearly on a Gr, Gs plot. For both cases, the general stability characteristics are similar, and the perturbation streamlines at onset are essentially the same.

The problem of calculating the onset of stability to the steady longitudinal modes can be transformed to the purely thermal problems of Hart (1972) and Kuo *et al.* (1986) as shown by Kerr in the Appendix.

3.3.1. $Le = 3$

For the thermal convection case, $Gs = 0$, the critical Gr is found to be 1942 with the critical wavenumber $k = 8.3$ – in agreement with the results of previous investigators. With the addition of a small γ_S at $Gs = 55$, the stability is enhanced somewhat with $Gr = 2200$ at the critical state due to the stabilizing vertical solute gradient in the upper and lower portions of the fluid layer. The marginal stability curve is shown in figure 7(*a*). At this low value of Gs, the unstable solute distribution in the middle portion of the fluid layer is not strong enough to cause any salt-finger instability. As Gs is increased to 60 (figure 7*b*), a small instability island emerges at a much reduced $Gr = 120$ with a smaller critical wavenumber $k = 3.0$. This is due to the

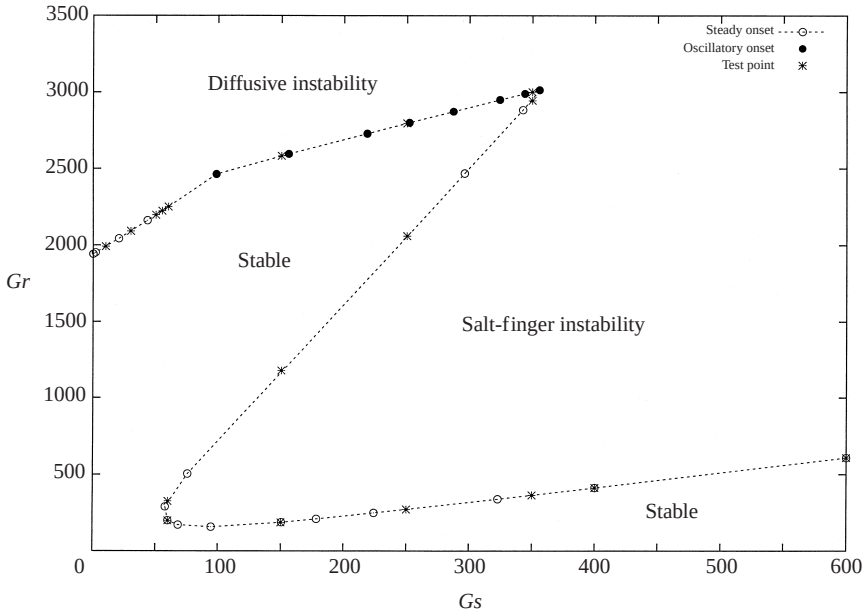

FIGURE 8. Stability map for the longitudinal mode in terms of Gr and Gs for $Le = 3$.

onset of salt-finger instability in the mid-portion of the fluid layer. A stable interval, $125 \leqslant Gr \leqslant 2200$, still remains. The thermal branch of the instability curve remains similar to the one at $Gs = 55$ but with a higher critical Gr. The finger instability island grows in area when Gs is increased to 150, as shown in figure 7(c), while the upper branch shows oscillatory onset due to the double-diffusive instability in the upper and lower portions of the fluid layer. The growth of the salt-finger instability island continues through $Gs = 250$ (figure 7d) until $Gs = 350$, when it is nearly in contact with the upper double-diffusive branch (figure 7e). At $Gs = 400$ (figure 7f), the double-diffusive and salt-finger branches become connected. Through this increase in Gs, the critical Grashof number Gr increases slightly while the critical wavenumber k remains at 3.0.

These results are summarized in figure 8, in which the critical Gr is shown as a function of Gs with regions of stability and instability clearly marked. The open circles denote steady onset and the filled circles denote oscillatory onset of instabilities. The stars denote the points for which detailed marginal stability curves have been constructed, six of which are shown in figure 7. For $50 \leqslant Gs \leqslant 350$, salt-finger instability, stable, and double-diffusive instability regions alternate as the imposed horizontal temperature gradient is increased. Beyond $Gs = 350$, salt finger is the only mode of instability. We note here that the basic flow is reversed and the circulation is clockwise for $Gs > Gr$. In this flow regime, a similar development of instabilities will occur. The onset point is at $Gr = 0$ and $Gs = 1942/Le$, when instability in the upper and lower portions of the fluid layer due to solute distribution alone will occur.

The perturbation streamlines in the (y, z)-plane at the marginal state for the onset of salt-finger instability are shown in figure 9 for the case $Gs = 95$, $Gr = 158$, and $k = 3.0$. The counter-rotating vortices are confined to the central portion of the fluid layer with the width of each vortex approximately equal to the height of the layer. The perturbed streamlines at the onset of double-diffusive instability at $Gs = 250$, $Gr = 2789$, and $k = 8.3$ are shown in figure 10. There are two rows of vortices along

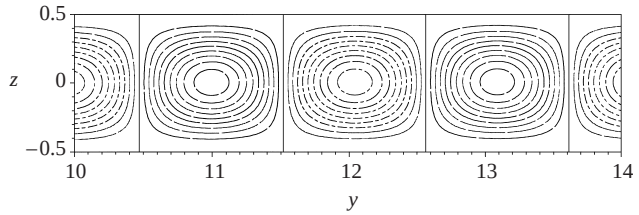

FIGURE 9. Perturbation streamlines in the longitudinal plane at the critical state for $Le = 3$, $Gs = 95$, $Gr = 158$, and $k = 3$. The instability is in the salt-finger mode.

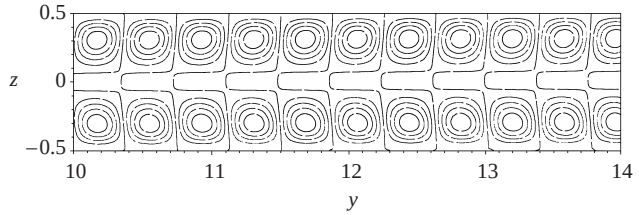

FIGURE 10. Perturbation streamlines in the longitudinal plane at the critical state for $Le = 3$, $Gs = 250$, $Gr = 2799$, and $k = 8.3$. The instability is in the diffusive mode with oscillatory onset.

the upper and lower portions of the fluid layer, with almost three vortices in the horizontal distance of the height of the layer.

3.3.2. $Le = 100$

For $Le = 100$, the flow becomes unstable at very low values of Gs. In order to maintain a steady basic flow, solute advection must be balanced by solute diffusion. To compensate for the drastically reduced value of the solute diffusion coefficient, the vertical solute gradient must be increased. This is evidenced by the fact that, in the basic flow, the solute variation is scaled with Le, equation (8). As a consequence, when the Lewis number is increased, the onset of salt-finger instability occurs at ever decreasing values of Gs. Furthermore, for a purely solute-driven convection, $Gr = 0$, the onset of buoyancy instability occurs at $Gs = 1942/Le = 19.4$ for $Le = 100$. This is shown in figure 11(a), where the marginal stability curve shows the critical Gr as a function of the wavenumber k. The upper branch is for the salt-finger instability while the instability region on the horizontal axis shows the onset of solutal buoyancy instability. Both instabilities onset to steady convection. As Gs is increased, the solutal buoyancy instability bubble grows, with the instability region enclosed by the curve. Note that the critical wavenumber for the salt-finger branch is 3.0 while the critical k for the solutal buoyancy branch is 8.3. The stable gap between the two branches becomes smaller and smaller as Gs is increased. The perturbation streamline plot for the salt-finger instability at the lowest Gr ($Gr = 4.83$ and $Gs = 1.93$) shows exactly the same pattern as that shown in figure 9 for the $Le = 3$ case.

The stability map for $Le = 100$ is shown in figure 12(a). Because of the much-reduced stable region, this map is presented in terms of $\log Gr$ versus $\log Gs$. The stability map for $Le = 3$ shown earlier in figure 8 is replotted in the logarithmic scale and presented here as figure 12(b) for the purpose of comparison. In both graphs, the diffusive instability region is denoted by A, the salt-finger instability region by B, the solute buoyancy instability region by C, and the stable region by D. It is seen that these two graphs have similar characteristics, with a much expanded unstable region

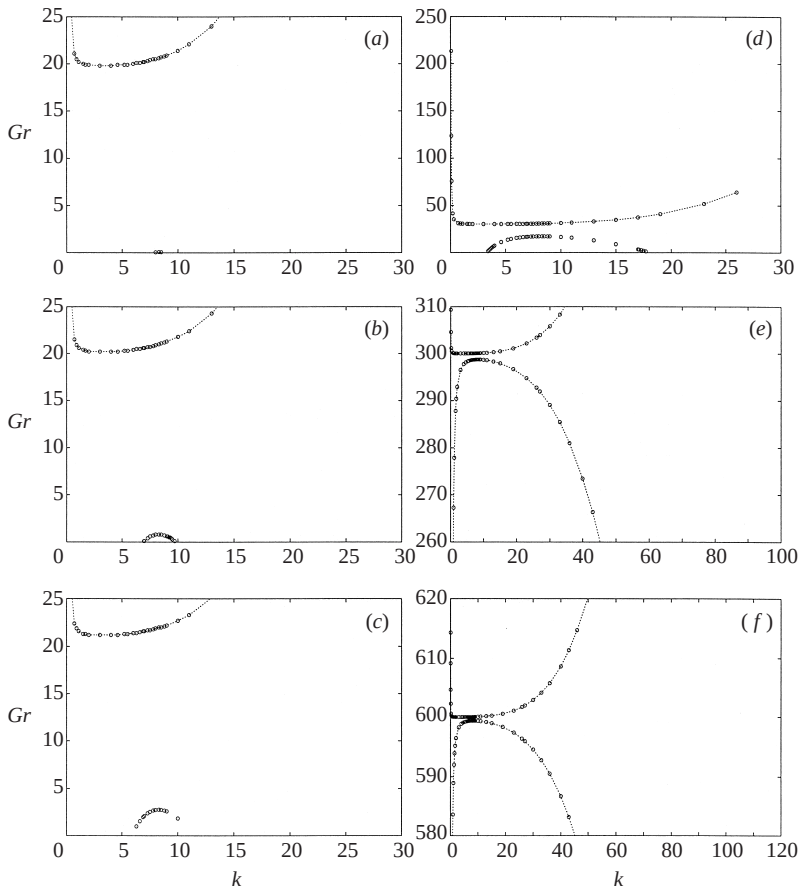

FIGURE 11. Marginal stability curves for the longitudinal mode for $Le = 100$ at increasing values of Gs: (*a*) 19.6, (*b*) 20, (*c*) 21, (*d*) 30, (*e*) 300, and (*f*) 600, showing the growth of the instability bubble arising for solutal instability when $Gs < Gr$.

for the $Le = 100$ case. In both graphs, the filled circles denote the stability boundary for $Gr > Gs$ and the crosses denote it for $Gr < Gs$. For $Le = 100$, figure 12(*a*), along the upper horizontal branch of the stability curve the instability onsets into steady convection for $Gs \leqslant 0.01$. For $0.01 < Gs < 0.049$, the onset is oscillatory because of double-diffusive effects. For $0.049 < Gs < 0.217$, there are alternating salt-finger instability, stable, and diffusive instability regions as Gr is increased. Beyond $Gs = 0.217$, the instability is in the salt-finger mode as long as $Gr > Gs$. The perturbation streamlines at onset are similar to those shown in figures 9 and 10 for the two modes of instability. For $Gs > 19.6$, the solutal buoyancy instability mode will become the most critical for the region $Gs > Gr$, while salt-finger instability is the most critical for the region $Gr > Gs$. For the experiments with the estimated values of $Gr = 1021$ and $Gs = 603$ and the appearance of only one row of vortices in the longitudinal plane within each convection cell, the instability we observed must be in the salt-finger mode.

3.4. *Results for the transverse mode*

The results of a stability analysis of the transverse mode for $Pr = 7$ and $Le = 3$ are shown in a $\log Gr$ versus $\log Gs$ graph in figure 13. In the same figure, the

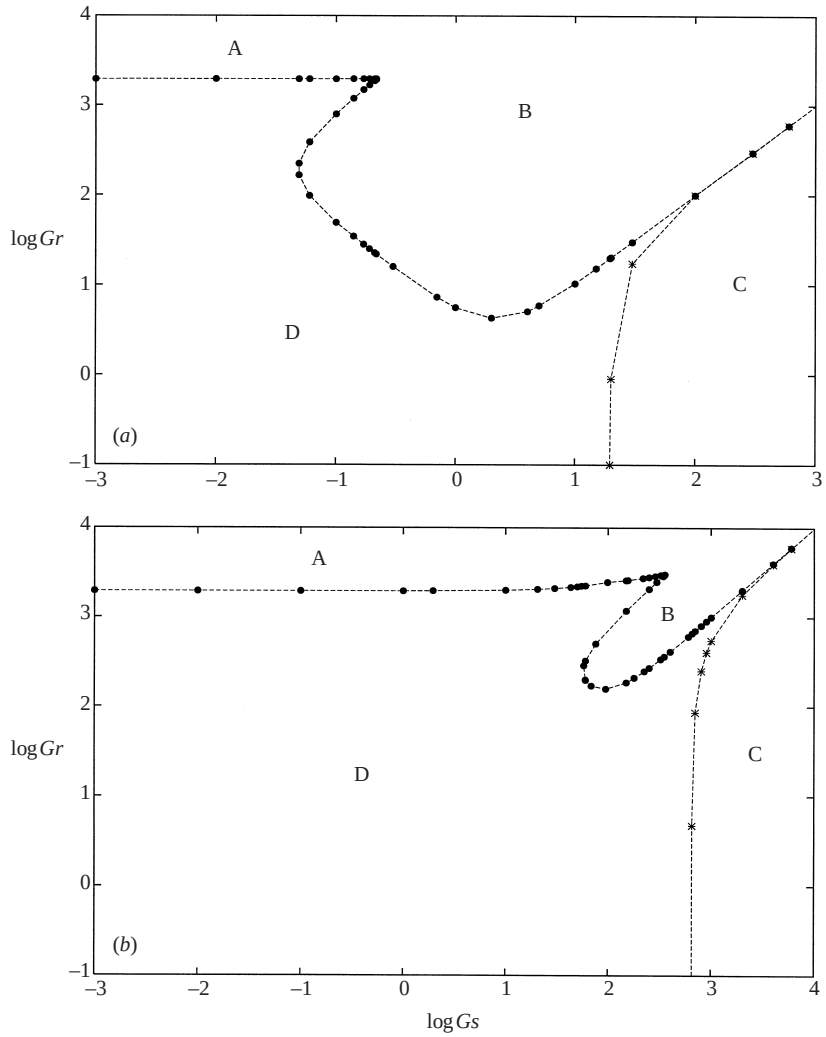

FIGURE 12. Stability map for the longitudinal mode in terms of log *Gr* and log *Gs* for (*a*) *Le* = 100 and (*b*) *Le* = 3. For both cases: region A = diffusive instability, region B = salt-finger instability; region C = solutal buoyancy instability; region D = stable region.

results for the longitudinal mode (figure 12*b*) are also shown for the purpose of comparison. The transverse mode is shown with filled circles while the longitudinal mode is open circles. It is seen that the stability boundaries for the transverse mode, similar to the longitudinal mode, delineate four separate regions: diffuse instability (A), finger instability (B), solute buoyancy instability (C), and stability (D). Unlike the longitudinal mode, the diffusive instability in the transverse mode onsets into oscillatory motion, even at $Gr = 0$. This is in agreement with results of Hart (1972) and Kuo *et al.* (1986) for $Pr > 0.14$.

We found the critical value of $Gr = 7037$ for the onset of transverse instability for $Gs = 0$. This value is approximately three times that found by Hart (1972) and Kuo *et al.* (1986) for the thermal convection case. It is well known from the results of Gallagher & Mercer (1965) and Ingersoll (1966) that the effect of shear greatly suppresses the transverse mode of instability in thermal convection compared to the

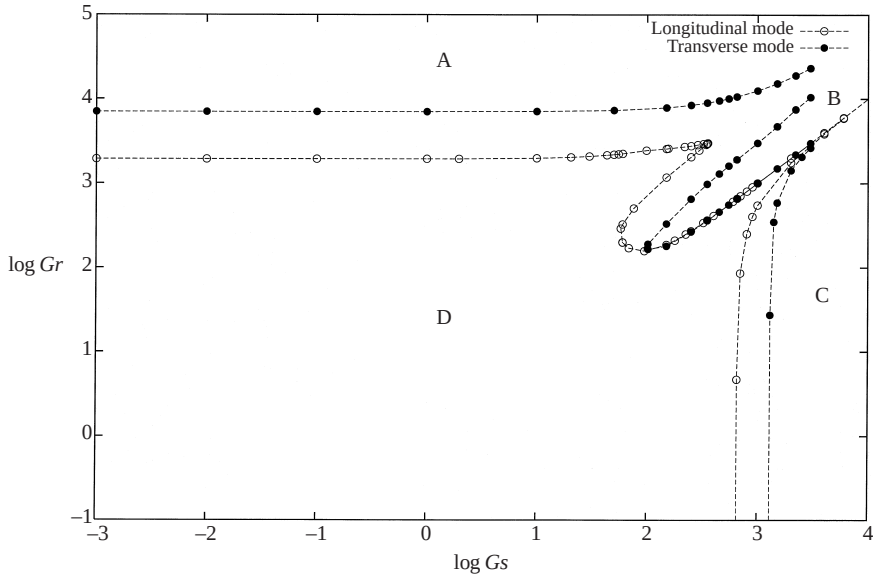

FIGURE 13. Stability map for the longitudinal and transverse modes for $Le = 3$ in terms of $\log Gr$ and $\log Gs$. Region A = diffusive instability, region B = salt-finger; region C = solutal buoyancy instability; region D = stable region.

longitudinal mode. It is surprising that the results of Hart (1972) and Kuo *et al.* (1986) show that the critical Grashof numbers for transverse and longitudinal instabilities are only slightly different from each. We checked our method of analysis by applying it to thermal convection in plane Couette flow. Our results for the small Reynolds number cases agreed very well with those obtained by using the asymptotic expression given by Ingersoll (1966).

The salt-finger instability region, indicated by B in figure 13, is similar to but smaller than that for the longitudinal mode. The critical conditions for the onset of finger instability are essentially the same for the transverse and the longitudinal modes, as suggested by Kerr (2000), who reasoned that salt-finger instability should not be influenced by shear in the same manner as the diffusive instability. The marginal state is nearly $Gr = Gs$; finger instability occurs when $Gr > Gs$. This conclusion will very likely remain true for $Le = 100$, as in the longitudinal mode, as shown in figures 12(a) and 12(b).

In our experimental observations, at the time when the vortices in the longitudinal plane are clearly in view, no comparable structures are seen in the transverse plane (see figures 3b and 3c). There are some faint circular streaklines in the transverse plane, as shown in figure 3(b). These may be the manifestations of finger instability somewhat masked by the primary circulation.

4. Summary and conclusions

The results of our experiments show that a secondary motion consisting of a row of vortices in the longitudinal plane with axes aligned in the direction of the temperature gradient appears shortly after the onset of primary convection cells. Velocity vectors obtained by PIV indicate that the speed of secondary motion is approximately one-half that of the primary motion. From the constant vorticity contours, the average

wavelength of the vortex pairs is approximately $0.8D$. This observation is consistent with the appearance of about 20 particle streaks in the horizontal plane of the experiments of Chen & Chen (1997).

A linear stability analysis is applied to a parallel flow model of a steady, double-diffusive convection in a long, horizontal shallow tank with imposed temperatures and solute concentrations at the two ends. The velocity, temperature, and concentration fields of this model flow for $Gr > Gs$ are similar to those measured by Chen & Chen (1997). The stability analyses were carried out for the longitudinal and transverse modes separately. In both modes, two types of instability characteristic of a double-diffusive system are excited, depending on the relative magnitudes of Gr and Gs. At low values of Gs, the instability is in the diffusive mode with oscillatory onset. The perturbation flow at onset consists of two rows of vortices. At higher values of Gs, the instability is in the salt-finger mode with steady onset. For this case, the perturbation flow at onset consists of a single row of vortices in the middle of each cell. For the longitudinal mode, the extent of the stable and unstable regions in the (Gr, Gs)-plane is greatly influenced by the value of the Lewis number. The stable region in the $Le = 100$ case is much smaller than in the $Le = 3$ case. However, the critical wavenumbers, k, of the two modes of instability remain constant, irrespective of the Lewis number, at $k = 8.3$ for the diffusive mode and at $k = 3.0$ for the salt-finger mode. For $Le = 100$, under any practical conditions, the flow is unstable. If $Gr > Gs$, as is the case in our experiments, the instability is in the salt-finger mode and, for $Gr < Gs$, the instability is in the solute buoyancy mode.

For the transverse mode, only the case for $Le = 3$ was considered. However, it is reasonable to expect similar behaviour as Le is increased to 100. Results of the stability analysis indicate that, at the experimental values of Gr and Gs, salt-finger instability will occur in both the longitudinal and transverse modes. The experimental particle traces and PIV velocity measurements give clear indications of vortices in the longitudinal plane but not in the transverse plane. This may be due to a combination of two factors. One is that the particle trace and velocity vectors in the transverse plane include both the primary and secondary motion, thus making the vortices harder to discern. The other is the possibility that the instability growth rate in the transverse mode is smaller than that in the longitudinal mode. A more sophisticated measurement and analysis of velocity vectors and a nonlinear stability analysis will provide more definitive answers to this apparent discrepancy between the experimental and theoretical results.

For $Le = 100$, the stability theory for the longitudinal mode predicts a critical wavelength of $\lambda = (2\pi/k)d = 2.09d$, which is more than twice that of the experimental value, $\lambda = 0.8d$. It was shown by Stern (1960) that the wavelength of the fastest growing salt-finger instability at a supercritical state is proportional to $(Gr\,Pr)^{-1/4}D$. Since the experiments were carried out at supercritical conditions, it is reasonable to expect the experimentally observed wavelength to be smaller than that predicted by the stability theory.

The following conclusions are reached:

1. A realistic simulation of the convection generated by sideways heating of a fluid stratified by a concentration gradient must be three-dimensional in nature in order to account for the secondary motion.

2. A linear stability analysis of a parallel flow model of the actual flow clarifies the physical mechanism causing the instability and predicts a flow pattern at onset in the longitudinal plane similar to the one observed in the experiment.

3. The theory predicts the critical wavelength at onset to be approximately twice that of the observed value. This can be explained by the fact that the fastest growing perturbation at the supercritical state has a wavelength that is proportional to $(Pr\,Gr)^{-1/4}D$.

We thank Mr. Youmin Yu for his help in performing the PIV analysis.

Appendix. Transformation of the model to the salt-free problem

By O. S. Kerr
Department of Mathematics, City University, Northampton Square, London EC1V 0HB, UK

When a salt-stratified body of fluid is heated from a sidewall almost horizontal convection layers can develop. These layers can undergo a secondary instability which takes the form of convection rolls aligned with their axes perpendicular to the walls (Chen & Chen 1997; Biello 1997). In the main paper further experiments are described and a model for these secondary instabilities devised. Each layer is modelled as a horizontal channel with imposed horizontal temperature and salinity gradients. With no salinity gradient this would be equivalent to the models of Hart (1972) and Kuo *et al.* (1986). We show that for steady marginal stability the model in the main paper for longitudinal modes can be transformed to the earlier salt-free problem. This is similar to transformations for double- and multiple-diffusive convection in a horizontal fluid layer (Knobloch 1980; Terrones 1993).

Using the notation and numbering of the main paper with $\sigma = 0$, we subtract $Gr/Gs\times$ equation (14) from (13) and define a new quantity $\hat{T} = T - Gs\,S/Gr$. We rescale u to give $\hat{u}$, defined by

$$\hat{u} = \frac{(Gr - Le\,Gs)u}{((Gr - Le^2Gs)(Gr - Gs))^{1/2}},$$

and define

$$\widehat{Pr} = \frac{(Gr - Le^2Gs)Pr}{Gr - Le\,Gs}, \quad \widehat{Gr} = \left(\frac{(Gr - Gs)(Gr - Le\,Gs)^2}{Gr - Le^2Gs}\right)^{1/2}.$$

This gives the equations for the stability of the purely thermal problem but with modified perturbation velocity component $\hat{u}$, Grashof number $\widehat{Gr}$ and Prandtl number $\widehat{Pr}$. It is clear that, since $Le > 1$, this transformation only works if either $Gr > Le^2Gs$ or $Gr < Gs$. This transformation can be used to calculate the boundaries corresponding to steady instabilities of regions A and C in figure 12 by solving the purely thermal problem.

For the case $Gs < Gr < Le^2Gs$ a similar transformation does exist with, for example $\widehat{Pr}$ being given by the magnitude of the above expression and the denominator in the fraction in the square root of the expression for $\widehat{Gr}$ being reversed. However the problem is mapped onto an unphysical problem with the vertical mean temperature gradient reversed, with cold fluid overlying warm fluid. The stability of this unphysical system can also be analysed, giving instabilities corresponding to the steady salt-finger instabilities of region B in figure 12. It should be noted that in the context of the model proposed in the main paper for the sidewall heating problem, Gr and Gs are not independent parameters.

REFERENCES

Biello, J. A. 1997 Aspects of double diffusion in a thin vertical slot. In *Double Diffuse Processes, 1996 Summer Study Programme in Geophysical Fluid Dynamics, Woods Hole Oceanog. Inst. Tech. Rep.* WHOI-97-10.

Chandrasekhar, S. 1961 *Hydrodynamic and Hydromagnetic Stability*, p. 635. Oxford University Press.

Chen, C. F. 1999 Convection generated by lateral heating of a solute gradient: review and extension. In *Fluid Dynamics at Interfaces* (ed. W. Z. Shyy & R. Narayanan), pp. 403–412. Cambridge University Press.

Chen, C. F., Briggs, D. G. & Wirtz, R. A. 1971 Stability of thermal convection in a salinity gradient due to lateral heating. *Int. J. Heat Mass Transfer* **14**, 57–65.

Chen, C. F. & Chen, F. 1997 Salt-finger convection generated by lateral heating of a solute gradient. *J. Fluid Mech.* **352**, 161–176.

Gallagher, A. P. & Mercer, A. M. 1965 On the behavior of small disturbances in plane Couette flow with a temperature gradient. *Proc. R. Soc. Lond.* A **286**, 117–128.

Hart, J. E. 1972 Stability of thin non-rotating Hadley circulation. *J. Atmos. Sci.* **29**, 687–697.

Huppert, H. E. & Turner, J. S. 1980 Ice blocks melting into a salinity gradient. *J. Fluid Mech.* **100**, 367–384.

Huppert, H. E., Kerr, R. C. & Hallworth, M. A. 1984 Heating or cooling in stable compositional gradient from the side. *Intl J. Heat Mass Transfer* **27**, 1395–1401.

Ingersoll, A. P. 1966 Convective instabilities in plane Couette flow. *Phys. Fluids* **9**, 682–689.

Jeevaraj, C. G. & Imberger, J. 1991 Experimental study of double-diffusive instability in sidewall heating. *J. Fluid Mech.* **222**, 565–586.

Kerr, O. S. 1992 Two-dimensional instabilities of steady double-diffusive interleaving. *J. Fluid Mech.* **242**, 99–116.

Kerr, O. S. 2000 Three-dimensional instability of steady double-diffusive interleaving. *J. Fluid Mech.* **418**, 297–312.

Knobloch, E. 1980 Convection in binary fluids. *Phys. Fluids* **23**, 1918–1920.

Kuo, H. P., Korpela, S. A., Chait, A. & Marcus, P. S. 1986 Stability of natural convection in a shallow cavity. In *Eighth Intl Heat Transfer Conf., San Francisco*, Vol. 4, pp. 1539–1544. Hemisphere.

Stern, M. E. 1960 The 'salt-fountain' and thermohaline convection. *Tellus* **12**, 172–175.

Terrones, G. 1993 Cross-diffusion effects on the stability criteria in a triply diffusive system. *Phys. Fluids* A **5**, 2172–2182.

Thorpe, S. A., Hutt, P. K. & Soulsby, R. 1969 The effects of horizontal gradients in thermohaline convection. *J. Fluid Mech.* **38**, 375–400.

Zuercher, E. J., Jacobs, J. W. & Chen, C. F. 1998 Experimental study of the stability of boundary layer flow along a heated inclined plate. *J. Fluid Mech.* **367**, 1–25.